Letter

Spin-phonon coupling suppressing the structural transition in perovskite-like oxide

Shalini Badola,[1] Supratik Mukherjee,[2] Greeshma Sunil,[1] B. Ghosh,[1] Devesh Negi,[1] G. Vaitheeswaran,[3,*] A. C. Garcia-Castro,[4,†] and Surajit Saha[1,‡]

[1]*Indian Institute of Science Education and Research Bhopal, Bhopal 462066, India*

[2]*Advanced Centre of Research in High Energy Materials, University of Hyderabad, Prof. C. R. Rao Road, Gachibowli, Hyderabad 500046, Telangana, India*

[3]*School of Physics, University of Hyderabad, Prof. C. R. Rao Road, Gachibowli, Hyderabad 500046, Telangana, India*

[4]*School of Physics, Universidad Industrial de Santander, Carrera 27 Calle 09, Bucaramanga 680002, Colombia*

(Received 18 May 2023; revised 6 September 2023; accepted 24 January 2024; published 29 February 2024)

Multifunctional properties in quantum systems require an interaction between different degrees of freedom. As such, spin-phonon coupling emerges as an ideal mechanism to tune multiferroicity, magnetism, and the magnetoelectric response. In this Letter, we demonstrate and explain, based on theoretical and experimental analyses, an unusual manifestation of spin-phonon coupling, i.e., prevention of a ferroelastic structural transition, and locking of the high-temperature $R\bar{3}m$ phase in a magnetically frustrated perovskitelike oxide Ba_2NiTeO_6. We present Ba_2NiTeO_6 as a prototype example among its family where a long-range antiferromagnetic structure couples with a low-frequency E_g mode (at $\sim$55 cm^{-1}) that exhibits a large anharmonicity. Our findings establish that spin-phonon coupling clearly suppresses the phonon anharmonicity, preventing the structural phase transition from the $R\bar{3}m$ to the $C2/m$ phase in Ba_2NiTeO_6.

DOI: 10.1103/PhysRevB.109.L060104

A nonlinear interaction between spins and phonons is critical not only for application-oriented phenomena such as multiferroicity, magnetoelectricity, superconductivity, etc., but to stabilize or melt specific magnetic and structural phases as well [1–7]. This has invigorated intense investigations on the cross-coupling between electron, spin, and phonon degrees of freedom in the realm of recent condensed matter research [8–11]. Spin-phonon coupling (SPC) provides a spin-relaxation channel to exchange energy between spin excitation and the thermal bath of the lattice [12]. Broadly, two fundamental mechanisms describe SPC in transition metal oxides. The conventional approach explains SPC mediating via an exchange pathway (J) modulated by the dynamical bond distance or bond angle during the vibration of the phonon mode [13]. Alternatively, it is understood through single-ion anisotropy that dominates in highly spin-orbit coupled $4d/5d$ systems [14]. Magnetic frustration is well known to further catalyze this coupling [15]. Thus, SPC manifests into physical phenomena that involve predominantly magnetism. Historically, spin-phonon coupling has been known to promote a structural transition/distortion, especially when there is magnetic frustration [4,16–19]. Moreover, in $SrMnO_3$, for example, SPC is responsible for the emergence of strain-induced multiferroicity [20–22]. Nevertheless, there are no studies so far, to the best of our knowledge, that establish SPC as a potential mechanism to prevent structural transition in transition metal oxides.

Perovskite Ba_2NiTeO_6 with a buckled honeycomb-type spin lattice offers an excellent platform to investigate SPC and its effect on the structural properties. The unique bilayer triangular arrangement of spins results in competing J's that induce strong magnetic frustration which eventually gets relieved to an antiferromagnetic (AFM) state below $T_N \sim 8.6$ K [23,24]. Unlike conventional transition metal oxides, Ba_2NiTeO_6 exhibits an unusual long-chain superexchange mediated via multiple ions in between the two nearest magnetic ions (Ni^{2+}). Consequently, SPC is expected to be extremely weak to cause any significant effect on the lattice dynamics. Ba_2NiTeO_6 crystallizes into trigonal symmetry ($R\bar{3}m$) that remains stable down to $\sim$2 K [24–26]. On the contrary, its isostructural nonmagnetic counterpart Ba_2ZnTeO_6 undergoes a concomitant ferroelastic and structural transition to a monoclinic phase ($C2/m$) below $\sim$150 K due to a soft mode instability arising from strong anharmonicity [27,28]. Thus, a distinction in the two structural dynamics despite their close similarities has remained a puzzle to date and needs to be addressed.

In this Letter, we demonstrate the crosstalk between magnetic and structural dynamics of Ba_2NiTeO_6 using Raman scattering, x-ray, and magnetic measurements as well as first-principles calculations. We find that most of the phonon modes deviate from the expected cubic-anharmonic trend below $\sim$100 K where a spin-spin short-ranged interaction emerges, indicating the onset of SPC. The SPC reduces the anharmonicity of the phonon mode at $\sim$55 cm^{-1} (which otherwise is a soft mode in Ba_2ZnTeO_6) and magnetic frustration in Ba_2NiTeO_6, thereby preventing the $R\bar{3}m$ to $C2/m$ structural transition [28].

All the experiments were performed on polycrystalline pellets of Ba_2NiTeO_6 and Ba_2ZnTeO_6 grown using the

*vaithee@uohyd.ac.in
†acgarcia@uis.edu.co
‡surajit@iiserb.ac.in

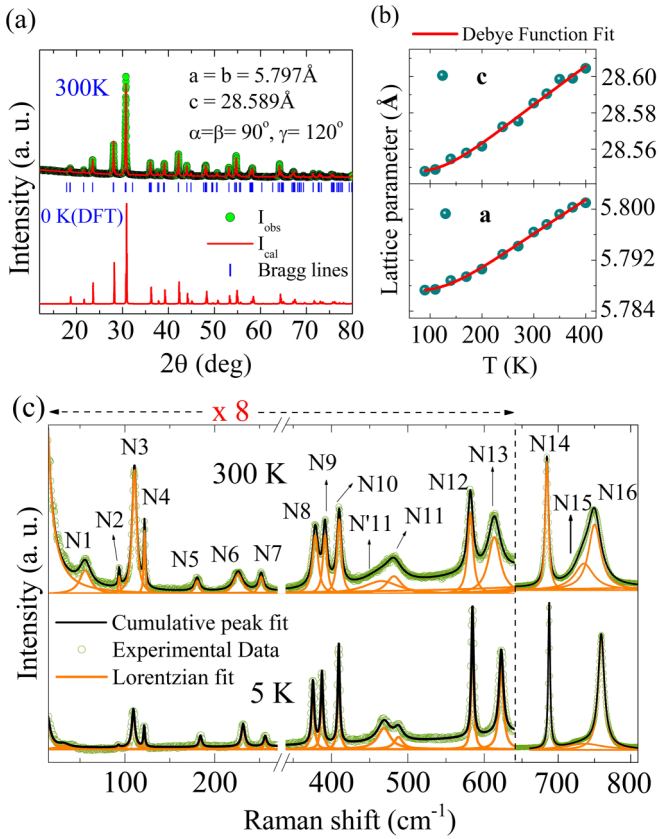

FIG. 1. (a) DFT calculated and room-temperature x-ray diffraction profiles of Ba_2NiTeO_6 displaying the lattice parameters. (b) Temperature evolution of the lattice parameters fitted (solid red line) using the Debye equation (see Supplemental Material [29]). (c) Raman spectra of Ba_2NiTeO_6 at a few temperatures showing deconvolutions of phonons as N1–N16 and N′11 at 300 K.

solid-state synthesis method as described in the Supplemental Material [29]. The experimentally recorded and density-functional theory (DFT)-calculated x-ray diffraction pattern of Ba_2NiTeO_6, shown in Fig. 1(a), confirm the trigonal crystal structure. The evolution of the lattice parameters with temperature was recorded by a PANalytical X-ray diffractometer attached to an Anton Paar TTK 450 heating stage, as shown in Fig. 1(b) [30]. The temperature evolution of the phonon modes was captured using an HR Evolution Raman spectrometer ($\lambda_{laser} = 532$ nm) coupled to an attoDRY 1000/SU cryostat and a Linkam heating stage (model HFS600E-PB4). Magnetic measurements were performed using a Quantum Design superconducting quantum interference device vibrating-sample magnetometer (SQUID-VSM). The experimental results were verified using first-principles calculations implemented in the VASP code [31–42]. The methods used are further detailed in the Supplemental Material [29].

Figure 1(c) presents the Raman spectra of Ba_2NiTeO_6 at ∼300 and ∼5 K. The spectra reveal a total of 16 Raman active modes N1–N16 ($9E_g + 7A_{1g}$), identified using a Lorentzian multifunction fit [see Fig. 1(c)]. The irreducible representation and the associated frequencies are included in Table SI in the Supplemental Material [29]. An additional broad band N′11 appears in the spectra at ∼450 cm^{-1} which is not expected as per group theory and may be assigned to disorder-induced Raman activity. Raman measurements show anomalies for most of the phonon modes appearing at intermediate temperatures (<100 K) where interatomic distances and magnetization also exhibit deviation from the expected trend (see Supplemental Material [29]). On the other hand, N1, N8, and N9 exhibit anomalous responses in frequency in the entire measured temperature range [refer to Figs. 2(a) and 2(b)], the origin of which is discussed later.

In general, various factors contribute to phonon anomalies over temperature (T) including spin-phonon, phonon-phonon, and electron-phonon couplings [43,44]. We analyze the T dependence of phonon frequencies (ω) illustrated in Fig. 2(a) using a standard cubic-anharmonic formalism given by [44]

$$\Delta\omega^{\text{canh}}(T) = \omega_0 + A\left(1 + \frac{2}{e^{x(T)} - 1}\right), \tag{1}$$

where $x(T) = \frac{\hbar\omega}{2k_BT}$ with $\hbar$ as the reduced Planck's constant and k_B as the Boltzmann coefficient. Moreover, ω_0 and A are the fitting parameters. $\Delta\omega^{\text{canh}}(T)$ expects the phonon frequency to decrease with increasing temperature. On the contrary, our analysis reveals that phonon frequencies in Ba_2NiTeO_6 deviate from $\Delta\omega^{\text{canh}}(T)$ at temperatures below ∼100 K. The insulating nature of the system excludes the possible contribution from electron-phonon coupling to cause this deviation. Therefore, we explore other possibilities to address the observed phonon anomalies.

Previous reports and our data suggest that Ba_2NiTeO_6 demonstrates a variety of magnetic properties, including magnetic frustration ($T_N < T < |\theta_{CW}|$), a short-ranged ordering (at ∼35 K), and an AFM order below T_N (∼8.6 K) [23,24]. A careful investigation of the magnetization data, displayed in Fig. 2(c), suggests that similar to the phonons, χ^{-1} also deviates from Curie-Weiss behavior below ∼100 K, implying a reduction in magnetic frustration and the onset of spin-spin correlation. We note that the temperature regime of phonon and magnetic anomalies largely coincides with each other. Therefore, temperature-dependent phonon anomalies below ∼100 K can be attributed to spin-phonon coupling. Since spin-spin correlations exist for this system even above the T_N, we combine Cottom and Lockwood's models along with the conventional mean-field approach to quantify the SPC constants (λ) (see Supplemental Material [29]) [44–48], which are found to be comparable to those in MnF_2, $HoCrO_3$, Ca_2RuO_4, Fe_3GeTe_2, and Ni_2NbBO_6 lying in the range of 0.3–1.5 cm^{-1}, as listed in Table I [46,49–52]. It may be noted that the modes N1, N8, and N9 exhibit anomalous softening upon cooling for the entire temperature range in our experiment. Therefore, these models may not be suitable for an accurate estimation of the values of λ for these modes. More details on the analysis of the spin-phonon coupling for N1, N8, and N9 modes can be found in Sec. V of the Supplemental Material [29]). We believe that such a coupling arises from an indirect superexchange interaction (Ni^{2+}-O^{2-}-Te^{6+}-O^{2-}-Ni^{2+}) mediated via corner- and/or face-shared TeO_6 octahedra, as discussed later.

Unlike other phonon modes, the cubic-anharmonic model could not explain the behavior of N1, N8, and N9 modes since their frequency decreases upon cooling in the entire temperature range [see Figs. 2(a) and 2(b)]. In particular, the

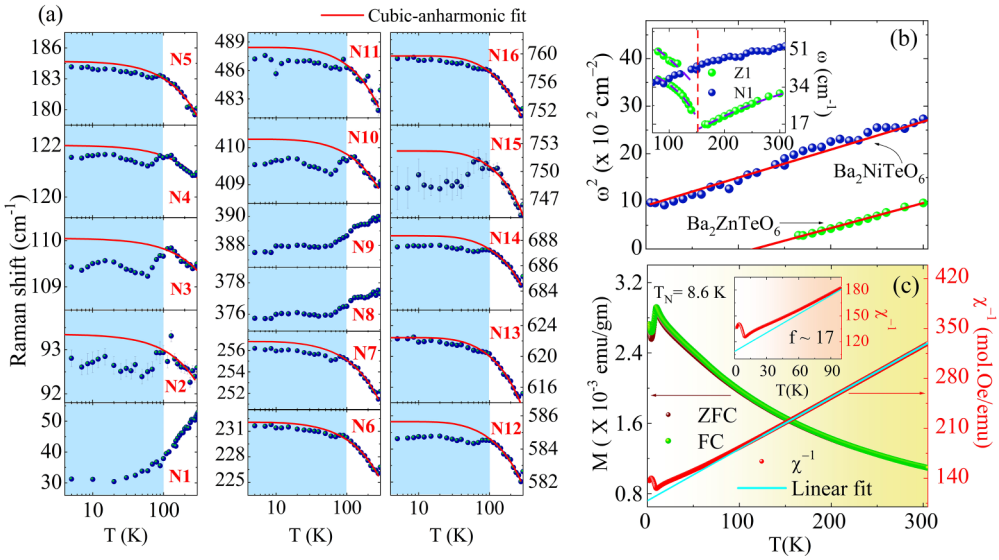

FIG. 2. (a) Phonon frequency as a function of temperature showing deviation from the cubic-anharmonic trend (solid red line) below 100 K. Error bars are included to show standard deviation in phonon frequencies. (b) Square of frequency (ω) of the phonon mode (N1/Z1) with temperature in isostructural systems Ba_2NiTeO_6 and Ba_2ZnTeO_6. Solid (red) lines are fit to Cochran's relation $\omega^2 = A(T - T_c)$. The inset shows the thermal response of phonon frequency of mode N1/Z1 across the transition temperature (shown with a vertical dashed red line) of Ba_2ZnTeO_6. (c) Temperature-dependent magnetization (M) and inverse susceptibility (χ^{-1}) of Ba_2NiTeO_6 showing $T_N \sim 8.6$ K. The inset shows χ^{-1} vs T representing an onset of deviation from the Curie-Weiss linear fit below 100 K.

lowest-frequency phonon mode N1 exhibits a large softening of $\frac{\Delta\omega}{\omega} = \frac{\omega(5\text{ K}) - \omega(300\text{ K})}{\omega(5\text{ K})} \sim -70\%$ upon cooling, as opposed to a typical hardening of ~1%–2% (see Sec. IV in the Supplemental Material for more details [29]). The fact that the contribution from SPC manifests only below intermediate temperatures (~100 K) and the electron-phonon coupling is absent, we ascribe the anomalous large softening of the phonon mode (N1) upon cooling ($T > 100$ K) to strong anharmonicity. In general, the total lattice anharmonicity [$\Delta\omega^{\text{canh}}(T)$] carries the contribution from both quasiharmonic and intrinsic anharmonic components. We estimate the quasiharmonic contribution to be small (~0.7%) for N1 from the temperature-dependent x-ray diffraction (see Supplemental Material [29]). This implies that a strong intrinsic phonon anharmonicity exists in Ba_2NiTeO_6 but does not lead to a structural transition such as the one in Ba_2ZnTeO_6.

TABLE I. The spin-phonon coupling coefficients, λ in cm^{-1}, extracted theoretically and experimentally for the Raman phonon modes in Ba_2NiTeO_6.

Mode (ω in cm^{-1})	$\lambda_{\text{expt.}}$	$\lambda_{\text{theor.}}$	Mode (ω in cm^{-1})	$\lambda_{\text{expt.}}$	$\lambda_{\text{theor.}}$
N1 (55)	[a]	34	N9 (391)	[a]	0.1
N2 (92)	0.7	0.1	N10 (409)	0.9	[a]
N3 (109)	0.8	1.6	N11 (482)	1.5	0.7
N4 (121)	0.6	0.1	N12 (581)	1.3	0.1
N5 (180)	0.6	0.2	N13 (613)	0.2	0.1
N6 (226)	0.5	1.3	N14 (684)	1.1	5.3
N7 (252)	0.8	[a]	N15 (746)	5.1	5.7
N8 (378)	[a]	0.9	N16 (752)	0.5	[a]

[a]Refer to text and Supplemental Material [29] for more details.

Unprecedented softening is typical of soft modes in the vicinity of the structural transition due to lattice anharmonicity. Similar to the soft mode Z1 (E_g) at ~30 cm^{-1} in Ba_2ZnTeO_6, we have modeled the phonon N1 (~55 cm^{-1}) in Ba_2NiTeO_6 with Cochran's relation $\omega^2 = A(T - T_c)$, as shown in Fig. 2(b) [27,28]. We find that Cochran's fit to N1 phonon frequency does not tend to zero at any finite temperature, unlike the mode Z1 in Ba_2ZnTeO_6. Therefore, N1 does not qualify to be a soft mode despite exhibiting a large softening. All these observations suggest that the phonon-phonon interactions may not be sufficient to drive a structural transition in Ba_2NiTeO_6, and it is important to consider the effects of other competing interactions (such as the active magnetic response).

In order to obtain an understanding of the distinction between the lattice dynamics of Ba_2NiTeO_6 and Ba_2ZnTeO_6, we made use of first-principles calculations, in the framework of density-functional theory, including different magnetic configurations. After full electronic and structural relaxation, the lattice parameters are found to be $a = b = c = 10.072$ Å and $\alpha = \beta = \gamma = 33.39^\circ$ in the trigonal primitive cell reference [see Fig. 3(a)]. These are equivalent to $a = b = 5.787$ Å, $c = 28.504$ Å, and $\alpha = \beta = 90.0^\circ$ and $\gamma = 120.0^\circ$ in the hexagonal unit cell reference and in full agreement with our experimentally measured values. In order to compute the coupling between the lattice dynamics and the magnetic structure, we have explored possible magnetic ground states in the Ba_2NiTeO_6. The ferromagnetic (FM) ordering was considered initially for reference followed by three different antiferromagnetic orderings, labeled as AFM1, AFM2, and AFM3 (see Supplemental Material [29]). In the AFM1 state, all the first neighbors are aligned antiferromagnetically and the propagation q vector can be represented as $q = (0, 0, 0)$ in the

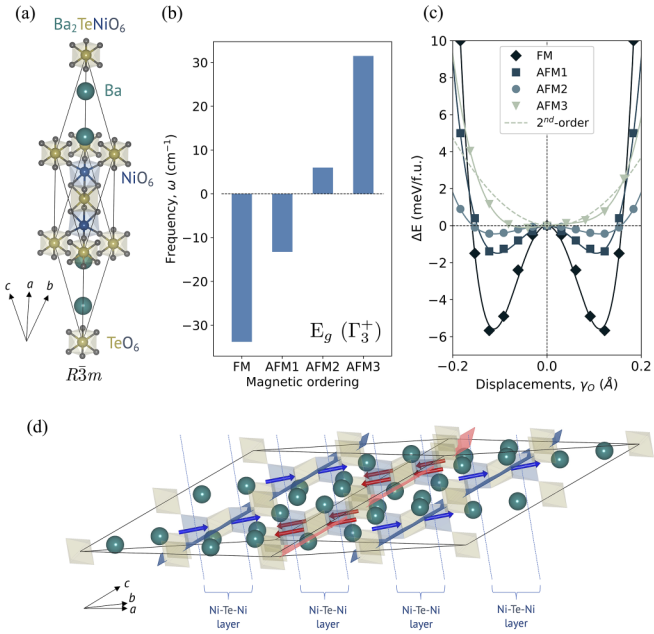

FIG. 3. (a) Primitive (1×1×1) structural unit cell of Ba_2NiTeO_6 without considering the magnetic ordering. (b) Calculated frequencies of the Γ_3^+ mode (N1) for different magnetic (FM, AFM1, AFM2, and AFM3) orderings with different propagation q vectors. The unstable (i.e., imaginary) frequencies are shown as negative values by notation. (c) Total energy wells obtained as a function of the rotational oxygen frozen displacements γ_O (i.e., condensation of the eigendisplacements associated with the N1 mode) and computed at different magnetic orderings. The latter total energy values are shown with reference to the undistorted structure. The displacements are measured as the averaged distortion of the oxygen sites involved in the octahedral rotation. (d) (2×2×2) supercell in which the corner-shared TeO_6 octahedra couple magnetism and phonon anharmonicity. The red and blue planes represent the magnetic planes in the AFM3 ordering. Additionally, the ferromagnetic NiO_6-TeO_6-NiO_6 path can be observed in the magnetic plane; meanwhile the antiferromagnetic interactions are mediated by the TeO_6 octahedra.

trigonal primitive cell (i.e., 20-atoms reference). In the AFM2 phase, the Ni-Ni interaction is ferromagnetic along Ni-Te-Ni face-shared octahedra (z axis) for the first two layers whereas the third layer is aligned antiferromagnetically. It can again be represented by a $q = (0, 0, 0)$ in the hexagonal unit cell (i.e., 60-atoms reference). Finally, the AFM3 state (akin to AFM2) shows a ferromagnetic alignment along the z axis in the Ni-Te-Ni octahedra. However, the overall magnetic structure is AFM along the [1,1,0] family of planes, as shown in the Supplemental Material [see Fig. S4(e)] [29]. As such, the AFM3 ordering can be considered with a $q = (1, 1, 0)$ magnetic propagation vector with respect to the (2×2×2) primitive unit cell reference and it is equivalent to the (0,0.5,1.0) q vector in the (1×2×1) hexagonal unit cell reference, consistent with the previous report by Asai *et al.* based on a neutron diffraction analysis [24]. The latter cells and orderings are shown in Fig. S4 in the Supplemental Material [29]. The full structural relaxation under all of the above magnetic orderings indicates that the AFM3 has the lowest-energy configuration, agreeing to the magnetic ground state predicted in Ref. [24].

After defining various magnetic ground states, we estimated the phonon frequencies at the Γ point considering each magnetic configuration. Interestingly, we obtained an unstable (i.e., negative frequency value by notation) phonon mode (N1) at 0 K associated with TeO_6 octahedral rotation with a Γ_3^+ irreducible representation. In the FM state, the phonon mode N1 shows a negative frequency of $\omega_{E_g} = -44\ \mathrm{cm}^{-1}$. Surprisingly, when the antiferromagnetic orderings (AFM1, AFM2, and AFM3) and larger magnetic cells are considered, the unstable phonon frequency is reduced and becomes stable, $\omega_{E_g} = 31\ \mathrm{cm}^{-1}$, for AFM3, as presented in Fig. 3(b). These observations confirm the strong correlation between phonon anharmonicity and magnetism in Ba_2NiTeO_6. The phonon mode (N1) is also observed in the isostructural compound Ba_2ZnTeO_6 in our previous work (labeled as Z1) [28] and is found to be responsible for the structural transition from $R\bar{3}m$ to the $C2/m$ crystal symmetry when the temperature is lowered. Nonetheless, as commented before, we do not observe the structural transition in our experiments and theoretical calculations for Ba_2NiTeO_6.

In order to establish coupling between phonon anharmonicity and magnetism, as indicated above, we have condensed or frozen the E_g (i.e., Γ_3^+) mode by including the eigendisplacements, associated with the phonon mode, into the high-symmetry $R\bar{3}m$ phase. As expected from the values of the unstable modes, the gain in energy in the energy-well profile is considerably reduced when larger magnetic cells are considered up to a point at which we obtain a single energy well for AFM3, indicating no gain in energy and a high-symmetry stable phase, as shown in Fig. 3(c). As in the FM, AFM1, and AFM2 cases, the energy well (i.e., ΔE vs γ_O) for the AFM3 phase is better fitted with the relations up to quartic terms. Further, to highlight the deviation of the obtained curve, we have also included the second-order fitting considering the quasiharmonic approximation. We find the quasiharmonic fitting relation as $\Delta E = (105.5\gamma^2 - 2.7\gamma)$ in contrast to the quartic relation $\Delta E = (4920.2\gamma^4 - 288.8\gamma^3 - 7.7\gamma^2 + 3.0\gamma)$. Note that the pure harmonic approximation implies $\Delta E \propto \gamma^2$. This highlights the importance of the quartic fourth-order terms supporting the strong anharmonicity of the Γ_3^+ mode in Ba_2NiTeO_6, as also observed in VO_2 [53] and ScF_3 [54]. As such, these results clearly indicate that the interactions between the spins and the lattice prevent the $R\bar{3}m$ to $C2/m$ phase transition in Ba_2NiTeO_6, as opposed to the one observed for the isostructural compound [28]. As a computational experiment, we also relaxed and computed the phonon modes in the nonmagnetic (NM) phase at 0 K. As expected, the Γ_3^+ is strongly unstable with a negative frequency value of $-385\ \mathrm{cm}^{-1}$ confirming that magnetic interactions are crucial to lock in the $R\bar{3}m$ phase through spin-phonon coupling in Ba_2NiTeO_6. Moreover, in terms of geometrical considerations and tolerance factor, the only (negligible) difference between the two compounds relies upon the atomic radius of Ni and Zn, which in the case of the 2+ oxidation state is almost identical with $r_{Ni} = 87$ pm and $r_{Zn} = 88$ pm, respectively [55]. This further ascertains spin-phonon coupling to be responsible for preventing the structural transition in Ba_2NiTeO_6.

We have included the calculated Raman frequencies for perovskite Ba_2NiTeO_6 considering the AFM3 magnetic ground state in the Supplemental Material [29]. The frequency values are in good agreement with our experimental Raman data. Moreover, the symmetry-mode assignment as well as the atomic species and atomic displacements involved are included for each mode. We have also estimated the spin-phonon coupling parameters (λ) for each of the modes, as listed in Table I (see more details in the Supplemental Material [29]). To computationally estimate the paramagnetic reference, we have taken the averaged FM, NM, AFM1, AFM2, and AFM3 frequency values as performed before for the MnF_2, ABF_3, and Mn_3NiN compounds [56–58]. Since different approaches are used for the estimation of λ in experiment and theory, it is likely to give a difference in their values which is considerable. Moreover, the difference in the values of λ can be reduced with the consideration of the short-ranged interaction in theory.

Finally, our experiments and calculations indicate that the rotation of the corner-shared TeO_6 octahedra [along with Ba/Ni(Zn) displacements], involved in the lowest-frequency phonon [N1 (Z1)], produces unprecedented anharmonicity. Interestingly, the same TeO_6 octahedra connect the antiferromagnetically aligned adjacent face-shared NiO_6-TeO_6-NiO_6 layers (Ni-Te-Ni layers) of Ba_2NiTeO_6 and mediate the superexchange interaction J through the Ni^{2+}-O^{2-}-Te^{6+}-O^{2-}-Ni^{2+} pathway to favor spin-phonon coupling [see Fig. 3(d)]. In this way, the structural stability of the $R\bar{3}m$ phase is ensured through entanglement (coupling) with the magnetic response in Ba_2NiTeO_6. The mediation of the spin-phonon coupling for the anomalous N8 and N9 modes is discussed in the Supplemental Material [29].

To conclude, an unconventional mechanism has been identified to prevent structural transition in Ba_2NiTeO_6 using temperature-dependent Raman spectroscopy, x-ray, and magnetic measurements as well as first-principles calculations. We observe phonon anomalies to appear well above the T_N ($\sim$8.6 K) wherein short-ranged magnetic interactions are initiated (below $\sim$100 K), depicting the onset of spin-phonon coupling. Our calculations establish the rare phenomena that spin-phonon coupling suppresses the strong phonon anharmonicity and magnetic frustration in Ba_2NiTeO_6, thereby preventing the $R\bar{3}m$ to $C2/m$ structural transition (unlike in Ba_2ZnTeO_6). We emphasize that exploring such coupled structural and magnetic phenomena (spin-phonon coupling) that can control phase transitions is important to induce multiferroic or magnetostrictive properties in nonmultiferroic systems, thus opening up alternate avenues.

S.S. acknowledges Science and Engineering Research Board (SERB) for funding through ECR/2016/001376 and CRG/2019/002668. Funding from DST-FIST [Project No. SR/FST/PSI-195/2014(C)], Nano-mission [Project No. SR/NM/NS-84/2016(C)], and Ministry of Education (Grant No. STARS/APR2019/PS/662/FS) are also acknowledged. D.N. acknowledges support via the fellowship [09/1020(0139)/2018-EMR-I] from CSIR. The authors acknowledge the Central Instrumentation Facility at IISER Bhopal for providing access to temperature-dependent XRD and SQUID-VSM facilities. Calculations presented in this Letter were carried out using the GridUIS-2 experimental testbed, being developed under the Universidad Industrial de Santander (SC3-UIS) High Performance and Scientific Computing Centre, development action with support from UIS Vicerrectoría de Investigación-y Extensión (VIE-UIS) and several UIS research groups as well as other funding resources. S.M acknowledges the financial support from DRDO, India, via ACRHEM (DRDO/18/1801/2016/01038:ACRHEM-PHASE-III). G.V. would like to acknowledge Institute of Eminence, University of Hyderabad (UOH-IOE-RC3-21-046) for the financial support and CMSD, University of Hyderabad for providing the Computational facility.

[1] M. Fiebig, T. Lottermoser, D. Meier, and M. Trassin, The evolution of multiferroics, Nat. Rev. Mater. **1**, 16046 (2016).

[2] W. S. Ferreira, J. Agostinho Moreira, A. Almeida, M. R. Chaves, J. P. Araújo, J. B. Oliveira, J. M. Machado Da Silva, M. A. Sá, T. M. Mendonça, P. Simeão Carvalho *et al.*, Spin-phonon coupling and magnetoelectric properties: $EuMnO_3$ versus $GdMnO_3$, Phys. Rev. B **79**, 054303 (2009).

[3] B. Keimer, S. A. Kivelson, M. R. Norman, S. Uchida, and J. Zaanen, From quantum matter to high-temperature superconductivity in copper oxides, Nature (London) **518**, 179 (2015).

[4] C. Cazorla, O. Diéguez, and J. Íñiguez, Multiple structural transitions driven by spin-phonon couplings in a perovskite oxide, Sci. Adv. **3**, e1700288 (2017).

[5] N. A. Spaldin and R. Ramesh, Advances in magnetoelectric multiferroics, Nat. Mater. **18**, 203 (2019).

[6] A. C. Garcia-Castro, W. Ibarra-Hernandez, E. Bousquet, and A. H. Romero, Direct magnetization-polarization coupling in $BaCuF_4$, Phys. Rev. Lett. **121**, 117601 (2018).

[7] A. C. Garcia-Castro, A. H. Romero, and E. Bousquet, Strain-engineered multiferroicity in *Pnma* $NaMnF_3$ fluoroperovskite, Phys. Rev. Lett. **116**, 117202 (2016).

[8] J.-J. Zhou, J. Park, I. Timrov, A. Floris, M. Cococcioni, N. Marzari, and M. Bernardi, *Ab initio* electron-phonon interactions in correlated electron systems, Phys. Rev. Lett. **127**, 126404 (2021).

[9] F. Ferrari, R. Valentí, and F. Becca, Effects of spin-phonon coupling in frustrated Heisenberg models, Phys. Rev. B **104**, 035126 (2021).

[10] H. Padmanabhan, M. Poore, P. K. Kim, N. Z. Koocher, V. A. Stoica, D. Puggioni, H. (Hugo) Wang, X. Shen, A. H. Reid, M. Gu, M. Wetherington, S. H. Lee, R. D. Schaller, Z. Mao, A. M. Lindenberg, X. Wang, J. M. Rondinelli, R. D. Averitt, and V. Gopalan, Interlayer magnetophononic coupling in $MnBi_2Te_4$, Nat. Commun. **13**, 1929 (2022).

[11] A. Bussmann-Holder, E. Liarokapis, and K. Roleder, Intriguing spin–lattice interactions in $EuTiO_3$, Sci. Rep. **11**, 18978 (2021).

[12] Y. Yafet, g factors and spin-lattice relaxation of conduction electrons, in *Solid State Physics* (Elsevier, Amsterdam, 1963), Vol. 14, pp. 1–98.

[13] S. Calder, J. Lee, M. B. Stone, M. D. Lumsden, J. Lang, M. Feygenson, Z. Zhao, J.-Q. Yan, Y. Shi, Y. Sun *et al.*, Enhanced spin-phonon-electronic coupling in a 5*d* oxide, Nat. Commun. **6**, 8916 (2015).

[14] C. H. Sohn, C. H. Kim, L. J. Sandilands, N. T. M. Hien, S. Y. Kim, H. J. Park, K. W. Kim, S. J. Moon, J. Yamaura, Z. Hiroi, and T. W. Noh, Strong spin-phonon coupling mediated by single ion anisotropy in the all-in–all-out pyrochlore magnet $Cd_2Os_2O_7$, Phys. Rev. Lett. **118**, 117201 (2017).

[15] C. Kant, J. Deisenhofer, T. Rudolf, F. Mayr, F. Schrettle, A. Loidl, V. Gnezdilov, D. Wulferding, P. Lemmens, and V. Tsurkan, Optical phonons, spin correlations, and spin-phonon coupling in the frustrated pyrochlore magnets $CdCr_2O_4$ and $ZnCr_2O_4$, Phys. Rev. B **80**, 214417 (2009).

[16] A. F. García-Flores, A. F. L. Moreira, U. F. Kaneko, F. M. Ardito, H. Terashita, M. T. D. Orlando, J. Gopalakrishnan, K. Ramesha, and E. Granado, Spin-electron-phonon excitation in Re-based half-metallic double perovskites, Phys. Rev. Lett. **108**, 177202 (2012).

[17] A. B. Sushkov, O. Tchernyshyov, W. Ratcliff, II, S. W. Cheong, and H. D. Drew, Probing spin correlations with phonons in the strongly frustrated magnet $ZnCr_2O_4$, Phys. Rev. Lett. **94**, 137202 (2005).

[18] J. Bartolomé, J. Rojo, R. Navarro, D. Gonzalez, M. Ibarra, and A. Del Moral, Magnetoelastic phase transition in $KMnF_3$, J. Magn. Magn. Mater. **31-34**, 1052 (1983).

[19] J. P. Pouget, L. P. Regnault, M. Ain, B. Hennion, J. P. Renard, P. Veillet, G. Dhalenne, and A. Revcolevschi, Structural evidence for a spin Peierls ground state in the quasi-one-dimensional compound $CuGeO_3$, Phys. Rev. Lett. **72**, 4037 (1994).

[20] J. H. Lee and K. M. Rabe, Large spin-phonon coupling and magnetically induced phonon anisotropy in $SrMO_3$ perovskites (M = V, Cr, Mn, Fe, Co), Phys. Rev. B **84**, 104440 (2011).

[21] J. H. Lee and K. M. Rabe, Epitaxial-strain-induced multiferroicity in $SrMnO_3$ from first principles, Phys. Rev. Lett. **104**, 207204 (2010).

[22] J. Hong, A. Stroppa, J. Íñiguez, S. Picozzi, and D. Vanderbilt, Spin-phonon coupling effects in transition-metal perovskites: A DFT+U and hybrid-functional study, Phys. Rev. B **85**, 054417 (2012).

[23] S. Asai, M. Soda, K. Kasatani, T. Ono, V. O. Garlea, B. Winn, and T. Masuda, Spin dynamics in the stripe-ordered buckled honeycomb lattice antiferromagnet Ba_2NiTeO_6, Phys. Rev. B **96**, 104414 (2017).

[24] S. Asai, M. Soda, K. Kasatani, T. Ono, M. Avdeev, and T. Masuda, Magnetic ordering of the buckled honeycomb lattice antiferromagnet Ba_2NiTeO_6, Phys. Rev. B **93**, 024412 (2016).

[25] M. Liegeois-Duyckaerts, Vibrational studies of molybdates, tungstates and related compounds-IV. Hexagonal perovskites: $Ba_2BIITeO_6$ (BII = Ni, Co, Zn), Spectrochim. Acta, Part A **31**, 1585 (1975).

[26] A. S. Gibbs, K. S. Knight, P. J. Saines, J. R. Hester, and H. Takagi, Phase diagrams of $Ba_2M^{2+}Te^{6+}O_6$: Insight into the interplay between crystal structure and magnetic dimensionality, Acta Crystallogr., Sect. A **72**, s61 (2016).

[27] R. L. Moreira, R. P. S. M. Lobo, S. L. L. M. Ramos, M. T. Sebastian, F. M. Matinaga, A. Righi, and A. Dias, Raman and infrared spectroscopic investigations of a ferroelastic phase transition in Ba_2ZnTeO_6 double perovskite, Phys. Rev. Mater. **2**, 054406 (2018).

[28] S. Badola, S. Mukherjee, B. Ghosh, G. Sunil, G. Vaitheeswaran, A. C. Garcia-Castro, and S. Saha, Lattice dynamics across the ferroelastic phase transition in Ba_2ZnTeO_6: A Raman and first-principles study, Phys. Chem. Chem. Phys. **24**, 20152 (2022).

[29] See Supplemental Material at http://link.aps.org/supplemental/10.1103/PhysRevB.109.L060104 for details of the analysis of interatomic bond distances using x-ray diffraction, estimation of the quasiharmonic term and spin-phonon coupling constants, magnetic susceptibility (χ^{-1}-T), calculated magnetic configurations, and phonon symmetry assignments in Ba_2NiTeO_6.

[30] C. Kittel and P. McEuen, *Introduction to Solid State Physics* (Wiley, Hoboken, NJ, 2018).

[31] P. Hohenberg and W. Kohn, Inhomogeneous electron gas, Phys. Rev. **136**, B864 (1964).

[32] W. Kohn and L. J. Sham, Self-consistent equations including exchange and correlation effects, Phys. Rev. **140**, A1133 (1965).

[33] G. Kresse and J. Furthmüller, Efficient iterative schemes for *ab initio* total-energy calculations using a plane-wave basis set, Phys. Rev. B **54**, 11169 (1996).

[34] G. Kresse and D. Joubert, From ultrasoft pseudopotentials to the projector augmented-wave method, Phys. Rev. B **59**, 1758 (1999).

[35] P. E. Blöchl, Projector augmented-wave method, Phys. Rev. B **50**, 17953 (1994).

[36] J. P. Perdew, A. Ruzsinszky, G. I. Csonka, O. A. Vydrov, G. E. Scuseria, L. A. Constantin, X. Zhou, and K. Burke, Restoring the density-gradient expansion for exchange in solids and surfaces, Phys. Rev. Lett. **100**, 136406 (2008).

[37] A. I. Liechtenstein, V. I. Anisimov, and J. Zaanen, Density-functional theory and strong interactions: Orbital ordering in Mott-Hubbard insulators, Phys. Rev. B **52**, R5467(R) (1995).

[38] H. J. Monkhorst and J. D. Pack, Special points for Brillouin-zone integrations, Phys. Rev. B **13**, 5188 (1976).

[39] X. Gonze and C. Lee, Dynamical matrices, Born effective charges, dielectric permittivity tensors, and interatomic force constants from density-functional perturbation theory, Phys. Rev. B **55**, 10355 (1997).

[40] A. Togo and I. Tanaka, First principles phonon calculations in materials science, Scr. Mater. **108**, 1 (2015).

[41] K. Kunc and R. M. Martin, *Ab initio* force constants of GaAs: A new approach to calculation of phonons and dielectric properties, Phys. Rev. Lett. **48**, 406 (1982).

[42] K. Momma and F. Izumi, Vesta 3 for three-dimensional visualization of crystal, volumetric and morphology data, J. Appl. Crystallogr. **44**, 1272 (2011).

[43] S. Saha, D. V. S. Muthu, S. Singh, B. Dkhil, R. Suryanarayanan, G. Dhalenne, H. K. Poswal, S. Karmakar, S. M. Sharma, A. Revcolevschi, and A. K. Sood, Low-temperature and high-pressure raman and x-ray studies of pyrochlore $Tb_2Ti_2O_7$: Phonon anomalies and possible phase transition, Phys. Rev. B **79**, 134112 (2009).

[44] M. Balkanski, R. F. Wallis, and E. Haro, Anharmonic effects in light scattering due to optical phonons in silicon, Phys. Rev. B **28**, 1928 (1983).

[45] J. Laverdière, S. Jandl, A. A. Mukhin, V. Y. Ivanov, V. G. Ivanov, and M. M. Iliev, Spin-phonon coupling in orthorhombic

$RMnO_3$ (R = Pr, Nd, Sm, Eu, Gd, Tb, Dy, Ho, Y): A Raman study, Phys. Rev. B **73**, 214301 (2006).

[46] D. Lockwood and M. Cottam, The spin-phonon interaction in FeF_2 and MnF_2 studied by Raman spectroscopy, J. Appl. Phys. **64**, 5876 (1988).

[47] M. Cottam and D. Lockwood, Spin-phonon interaction in transition-metal difluoride antiferromagnets: Theory and experiment, Low Temp. Phys. **45**, 78 (2019).

[48] E. Aytan, B. Debnath, F. Kargar, Y. Barlas, M. Lacerda, J. Li, R. Lake, J. Shi, and A. Balandin, Spin-phonon coupling in antiferromagnetic nickel oxide, Appl. Phys. Lett. **111**, 252402 (2017).

[49] G. Kotnana, V. G. Sathe, and S. Narayana Jammalamadaka, Spin–phonon coupling in $HoCr_{1-x}Fe_xO_3$ ($x = 0$ and 0.5) compounds, J. Raman Spectrosc. **49**, 764 (2018).

[50] M.-C. Lee, C. H. Kim, I. Kwak, C. W. Seo, C. Sohn, F. Nakamura, C. Sow, Y. Maeno, E.-A. Kim, T. W. Noh, and K. W. Kim, Strong spin-phonon coupling unveiled by coherent phonon oscillations in Ca_2RuO_4, Phys. Rev. B **99**, 144306 (2019).

[51] L. Du, J. Tang, Y. Zhao, X. Li, R. Yang, X. Hu, X. Bai, X. Wang, K. Watanabe, T. Taniguchi *et al.*, Lattice dynamics, phonon chirality, and spin–phonon coupling in 2D itinerant ferromagnet Fe_3GeTe_2, Adv. Funct. Mater. **29**, 1904734 (2019).

[52] M. A. Prosnikov, A. N. Smirnov, V. Y. Davydov, R. V. Pisarev, N. A. Lyubochko, and S. N. Barilo, Magnetic dynamics and spin-phonon coupling in the antiferromagnet Ni_2NbBO_6, Phys. Rev. B **98**, 104404 (2018).

[53] J. D. Budai, J. Hong, M. E. Manley, E. D. Specht, C. W. Li, J. Z. Tischler, D. L. Abernathy, A. H. Said, B. M. Leu, L. A. Boatner, R. J. McQueeney, and O. Delaire, Metallization of vanadium dioxide driven by large phonon entropy, Nature (London) **515**, 535 (2014).

[54] C. W. Li, X. Tang, J. A. Muñoz, J. B. Keith, S. J. Tracy, D. L. Abernathy, and B. Fultz, Structural relationship between negative thermal expansion and quartic anharmonicity of cubic ScF_3, Phys. Rev. Lett. **107**, 195504 (2011).

[55] R. Shannon, Revised effective ionic radii and systematic studies of interatomic distances in halides and chalcogenides, Acta Cryst. **A32**, 751 (1976).

[56] R. Schleck, Y. Nahas, R. P. S. M. Lobo, J. Varignon, M.-B. Lepetit, C. S. Nelson, and R. L. Moreira, Elastic and magnetic effects on the infrared phonon spectra of MnF_2, Phys. Rev. B **82**, 054412 (2010).

[57] R. M. Dubrovin, A. C. Garcia-Castro, N. V. Siverin, N. N. Novikova, K. N. Boldyrev, A. H. Romero, and R. V. Pisarev, Incipient geometric lattice instability of cubic fluoroperovskites, Phys. Rev. B **104**, 144304 (2021).

[58] L. Flórez-Gómez, W. Ibarra-Hernández, and A. Garcia-Castro, Lattice dynamics and spin–phonon coupling in the noncollinear antiferromagnetic antiperovskite Mn_3NiN, J. Magn. Magn. Mater. **562**, 169813 (2022).